Extension of the Exergy Balance to Rotating Frames of Reference: Application to a Propeller Configuration

Ilyès Berhouni, Didier Bailly, Ilias Petropoulos

Extension of the Exergy Balance to Rotating Frames of Reference: Application to a Propeller Configuration

Ilyès Berhouni*, Didier Bailly†, Ilias Petropoulos‡
ONERA - The French Aerospace Lab, Meudon, F-92190, France

The exergy analysis for aerospace applications already proved to be of interest, with the possibility to numerically analyze new types of configurations. It is of particular interest when a relevant thrust/drag breakdown is not possible and when significant thermal exchanges occur in the control volume. It also allows to link the different contributions of the exergy terms to physical phenomena in the flow, allowing to improve the understanding of the sources of losses degrading the performance of the system under study. The applications and results obtained in a fixed frame of reference motivated the improvement and extension of the exergy balance to more complex flows. This paper aims at presenting an extension of the exergy balance to rotating frames of reference in order to be able to study rotating components of the propulsion system in detail (e.g. propeller, turbomachine or helicopter rotor blades). The newly developed theoretical development is summarized, and an application to a numerical simulation of a propeller is presented. The precision of the results obtained is also analyzed.

I. Nomenclature

$\dot{\mathcal{A}}_w$	=	Rate of anergy generation by shockwaves, J.s^{-1}
$\dot{\mathcal{A}}_{\nabla T}$	=	Rate of anergy generation by thermal mixing, J.s^{-1}
$\dot{\mathcal{A}}_\phi$	=	Rate of anergy generation by viscous dissipation, J.s^{-1}
$\dot{\mathcal{A}}_{tot}$	=	$\dot{\mathcal{A}}_\phi + \dot{\mathcal{A}}_{\nabla T} + \dot{\mathcal{A}}_w$, Rate of total anergy generation, J.s^{-1}
C	=	Transformation matrix between a fixed and a rotating frame
E	=	Mass specific total energy, J.kg^{-1}
$\dot{E}_u$	=	Streamwise kinetic energy deposition rate, J.s^{-1}
$\dot{E}_v$	=	Transverse kinetic energy deposition rate, J.s^{-1}
$\dot{E}_p$	=	Boundary pressure-work rate, J.s^{-1}
$\dot{\mathcal{E}}_m$	=	Rate of mechanical exergy outflow, J.s^{-1}
$\dot{\mathcal{E}}_{prop}$	=	Rate of exergy supplied by the propulsion system, J.s^{-1}
$\dot{\mathcal{E}}_q$	=	Rate of heat exergy supplied by conduction, J.s^{-1}
$\dot{\mathcal{E}}_{th}$	=	Rate of thermal exergy outflow, J.s^{-1}
H	=	Mass specific total enthalpy, J.kg^{-1}
M	=	Mach number
OM	=	Position vector
Re	=	Reynolds number
R_p	=	Propeller radius, m
S_b	=	Body surface
S_O	=	Outer boundary of the control volume
T	=	Static temperature, K
$\mathbf{V}$	=	$(V_\infty + u)\mathbf{x}$, $v\mathbf{y}$, $w\mathbf{z}$, Fluid velocity vector, m.s^{-1}
$W\dot{\Gamma}$	=	Power consumed by the body to maintain its current axial equilibrium, J.s^{-1}
$W\dot{\Omega}$	=	Power transferred from the solid body to the flow through the torque available, J.s^{-1}
e	=	Mass specific internal energy, J.kg^{-1}
h	=	Mass specific enthalpy, J.kg^{-1}

*Ph.D. student, ONERA Department of Aerodynamics, Aeroelasticity and Acoustics, ilyes.berhouni@onera.fr.
†Research Scientist, Ph.D., ONERA Department of Aerodynamics, Aeroelasticity and Acoustics, didier.bailly@onera.fr.
‡Research Scientist, Ph.D., ONERA Department of Aerodynamics, Aeroelasticity and Acoustics, ilias.petropoulos@onera.fr.

k = Thermal conductivity, $W.m^{-1}.K^{-1}$
$\mathbf{n}$ = Unit normal vector
$\tilde{\mathbf{n}}$ = Unit normal vector on the shock wave surface
p = Static pressure, $kg.m.s^{-2}$
pc = Power counts (10^{-4})
$\mathbf{q}$ = Heat flux by conduction, $J.s^{-1}$
s = Mass specific entropy, $J.K^{-1}.kg^{-1}$
$\mathbf{s_e}$ = $\boldsymbol{\omega} \times \mathbf{OM}$, Rotating velocity, $m.s^{-1}$
$\delta(\ )$ = Quantity relative to the freestream, = $(\ ) - (\ )_\infty$
ϵ = Mass specific exergy, $J.kg^{-1}$
ϵ_{flow} = Mass specific flow exergy, $J.kg^{-1}$
μ = Fluid dynamic viscosity, $kg.m.s^{-1}$
ρ = Density, $kg.m^{-3}$
$\overline{\overline{\tau}}$ = Viscous stress tensor, N
ϕ = Dissipation rate per unit volume, $J.s^{-1}.m^{-3}$
$\boldsymbol{\omega}$ = Angular velocity, $rad.s^{-1}$
$(\ )_\infty$ = Quantity $(\ )$ at freestream conditions
$(\ )'$ = Quantity $(\ )$ projected in the relative frame, = $C^T(\ )$
$:=$ = Equal by definition
$[\![\ ]\!]$ = Discontinuous jump of a quantity
$\frac{d}{dt}_{\mathbf{s_e}}$ = Material derivative of a quantity expressed in the velocity field $\mathbf{s_e}$

II. Introduction

Ever since the first commercial flights, the search for better aircraft efficiency has been a leading factor that motivated the evolution of aircraft. The reduction of carbon dioxide emissions has since become a significant goal for many countries. Due to the raising objectives for the reduction of greenhouse gas emissions which came with stimulus plans, the aviation sector has to keep evolving faster in order to reach better results in terms of pollutant releases. However, such rapid improvements imply the development of disruptive technologies, as this gain of efficiency must come from all areas of development of aircraft, such as the external aerodynamic efficiency, the source of energy and the effectiveness of the propulsion systems involved.

In this context, new configurations allowing a better aerodynamic efficiency like the Boundary Layer Ingestion (BLI) concept are considered to be promising. In order to be able to analyze the performance of such configurations where the separation between thrust and drag is not as obvious as for the tube and wing configurations, the need for new theoretical and numerical models has emerged. Indeed, classical force-based models evaluating the different drag components [1] [2] are less adapted to evaluate the performance of such new concepts. In order to tackle this problem, a first new approach based on a mechanical energy analysis for transonic to supersonic aircraft was proposed by Drela [3]. This approach avoids the need for a thrust/drag separation that appears with force-based analyses, and still allows to quantify the influence of the different phenomena in the flow that are of interest in the process of designing an aircraft, such as shockwaves, wakes and lift-induced vortices.

The power-balance approach of Drela allows to study new configurations such as BLI from a mechanical point of view, but does not take into account thermal effects. This motivated the development of another approach at ONERA based on the concept of exergy, which corresponds to the maximum theoretical work that can be extracted from the system under study, thermal or mechanical. This formulation was developed by Arntz [4] [5] and allowed to link the different components of the balance to physical phenomena, with a separation between the exergy provided to the system, the part of it that is consumed, the exergy leaving the system (i.e. wasted in terms of potential for thrust production) and the anergy generated, corresponding to the exergy destroyed by irreversible phenomena. This formulation was successfully applied to conventional and disruptive configurations of aircraft [5], studied and improved numerically [6] over the last years.

The latest formulation can be applied to aircraft configurations in a fixed reference frame, but does not sufficiently cover rotating configurations. An exergy balance adapted to such cases was investigated by Fiore [7] and applied to a linear cascade and a two-stage annular cascade configuration. However, the equations were not written in their arbitrary Lagrangian-Eulerian form and the final decomposition did not let the momentum conservation equation or the different

components of exergy outflow appear explicitly. As a consequence the inertial terms appearing for a rotating frame of reference could not appear explicitly. Furthermore, the absence of the use of the momentum equation does not allow to explicitely describe the power consumed to maintain the current axial equilibrium (which can be further linked to drag and thrust). The point of view adopted was different than the one used by Arntz: the latest gives a clearer link between some far-field terms of the final exergy balance and physical phenomena appearing in the near-field.

The special case of rotating frames is of interest when considering turbomachines such as propellers or turbofans, as the exergy balance could be used to localize sources of loss with the goal to optimize such configurations. The benefits of the exergy concept are even greater for configurations with significant thermal exchanges, as this aspect is not adequately captured by force-based approaches.

This paper aims at presenting the development of the exergy balance for rotating frames and its application to a propeller configuration through the post-processing code FFX (Far-Field Exergy) developed and used at ONERA. The theoretical derivation is detailed in Sec. III, and results highlighting the interest of the exergy balance in the case of a propeller analysis are presented in Sec. IV. The precision of the results and the reasons for the errors that can be observed are also discussed.

III. Exergy balance for rotating frames of reference

A. System definition

The fluid flow analysis is carried out in a continuous volume $\mathcal{V}$ delimited by a solid body surface S_b and an outer boundary S_O, as illustrated in Fig. 1. The control volume follows the movement of the body which is in rotation at a velocity $\mathbf{s_e}$ with respect to the inertial fixed frame R_A, and a non-inertial relative frame R_r is attached to it. A vector pointing outwards of the volume and locally normal to the surface is noted $\mathbf{n}$. Since the volume follows the movement of the body with the same velocity $\mathbf{s_e}$, a steady-state assumption is considered in the relative frame. The presence of a steady shockwave attached to the body is also considered through a surface of discontinuity $\tilde{S}_w$, with a corresponding normal vector $\tilde{\mathbf{n}}$ pointing towards the exterior of the volume $\mathcal{V}$.

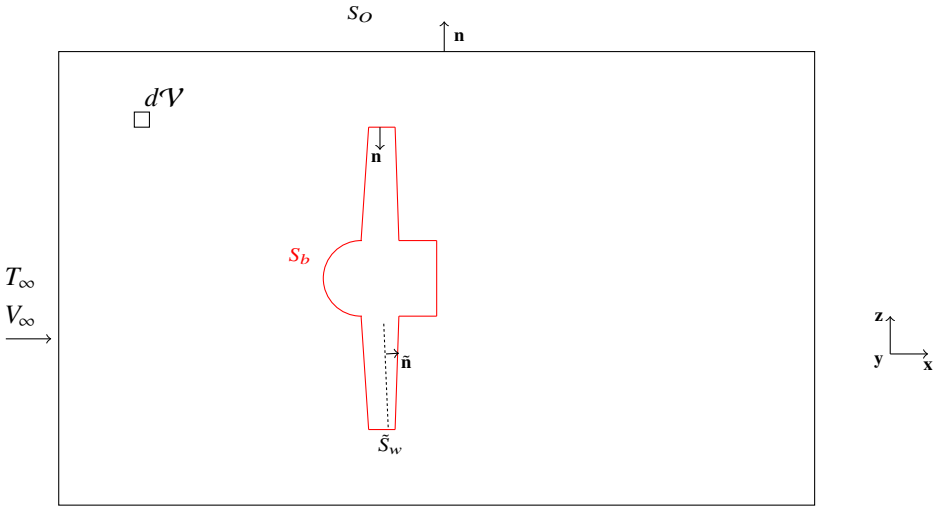

Fig. 1 2D cut of a 3D control volume surrounding a solid body in rotation.

The system is thermodynamically open as it can exchange mass, work and heat with the surrounding fluid across its boundaries. The atmosphere is considered as a thermal and mechanical reservoir surrounding the control volume and also corresponds to the reference (or dead) state in the exergy definition that will be detailed in a further section. The analysis is carried out in the body's reference frame, which is non-inertial, and the control volume is therefore fixed in the rotating frame with the air flowing in and out of it. In this figure, the near-field surface has been chosen as the rotating body's surface, giving the null relative velocity as the wall condition, i.e. $(\mathbf{V}' - \mathbf{s_e}') = \mathbf{0}$ on S_b.
Three hypotheses are made in the rest of this paper:

- The flow is steady in the rotating frame.

- The air is considered a perfect gas.
- $\mathbf{V}' = (V'_\infty + u', v', w')^T$, i.e. the reference state velocity is defined along the rotation axis and the velocity perturbations in the rotating frame are noted u',v' and w'.

B. Equations of interest expressed in the rotating frame

1. Choice of the formulation

When writing the equations of fluid dynamics in a rotating frame, there are several possibilities. In this case, the goal is to be able to consider the system as steady in the rotating frame with the corresponding simplifications for the equations, which can be achieved by writing the equations in the Arbitrary Lagrangian-Eulerian (ALE) form. There are two well-known possibilities that were considered for this study and are well detailed by Boniface [8] and Kozuch [9]: for both options, one has to project all quantities in the relative frame, but then the equations can be written as functions of the absolute velocity or as functions of the relative velocity. These two formulations are strictly equivalent, but allow to describe the physics of the flow differently as they respectively describe it from a fixed referential and from the relative one.

In this paper, the first formulation is selected and is referred to as the absolute velocity, relative frame formulation. This is done in order to be consistent with the equations solved in the Computational Fluid Dynamics (CFD) solver, although the other formulation is still of interest and could be studied in the future. Hence, the exergy balance and all the equations used in order to derive it will be written in their absolute velocity, relative frame form.

2. Conservation equations in a rotating frame

With the steady-state assumption in the rotating frame, the mass, momentum and energy integral equations can be written as follows in their absolute velocity, relative frame form:

$$\int_{\partial\mathcal{V}} \rho(\mathbf{V}' - \mathbf{s_e}') \cdot \mathbf{n}' \, \mathrm{d}S = 0 \tag{1}$$

$$\boldsymbol{\omega}' \times \int_{\mathcal{V}} \rho \mathbf{V}' \, \mathrm{d}\mathcal{V} + \int_{\partial\mathcal{V}} (\rho \mathbf{V}' \otimes (\mathbf{V}' - \mathbf{s_e}') + (p\overline{\overline{I}}' - \overline{\overline{\tau}}')) \cdot \mathbf{n}' \, \mathrm{d}S = \mathbf{0} \tag{2}$$

$$\int_{\partial\mathcal{V}} (\rho \delta E(\mathbf{V}' - \mathbf{s_e}') + \mathbf{q}' + (p\overline{\overline{I}}' - \overline{\overline{\tau}}') \cdot \mathbf{V}') \cdot \mathbf{n}' \, \mathrm{d}S = 0 \tag{3}$$

The mass and energy conservation equations are very similar to those expressed in the fixed frame, with the only difference being that the relative velocity $(\mathbf{V}' - \mathbf{s_e}')$ appears in the mass and energy flow terms. This stays true for the momentum equation, but as it is a vectorial equation an inertial term $\boldsymbol{\omega}' \times \int_{\mathcal{V}} \rho \mathbf{V}' \, \mathrm{d}\mathcal{V}$ appears as a result of the rotational effect.

In addition to these three equations, the torque conservation equation is considered in its integral form:

$$\int_{\partial\mathcal{V}} ((\mathbf{OM} \times \rho\mathbf{V})'(\mathbf{V}' - \mathbf{s_e}') + (\mathbf{OM} \times ((p - p_\infty)\overline{\overline{I}} - \overline{\overline{\tau}}))') \cdot \mathbf{n}' \, \mathrm{d}S + \boldsymbol{\omega}' \times \int_{\mathcal{V}} (\mathbf{OM} \times \rho\mathbf{V})' \, \mathrm{d}\mathcal{V} = \mathbf{0} \tag{4}$$

By multiplying Eq. (2) with $\mathbf{V}'_\infty$ and Eq. (4) with $\boldsymbol{\omega}'$, two quantities are introduced:

$$W\dot{\Gamma}' = \int_{S_O} (\rho u' V'_\infty (\mathbf{V}' - \mathbf{s_e}') + (p - p_\infty)\mathbf{V}'_\infty - (\overline{\overline{\tau}}' \cdot \mathbf{V}'_\infty)) \cdot \mathbf{n}' \, \mathrm{d}S + \mathbf{V}'_\infty \cdot \cancel{\int_{\mathcal{V}} \rho \boldsymbol{\omega}' \times \mathbf{V}' \, \mathrm{d}\mathcal{V}} \tag{5}$$

$$W\dot{\Omega}' = -\int_{S_b} ((p - p_\infty)(\mathbf{s_e}' \cdot \mathbf{n}') - (\overline{\overline{\tau}}' \cdot \mathbf{s_e}') \cdot \mathbf{n}') \, \mathrm{d}S \tag{6}$$

which are respectively the power consumed by the body to maintain the current axial equilibrium and the power transmitted from the solid body to the flow through the torque available. The second term of Eq. (5) is cancelled due to the reference velocity being parallel to the axis of rotation, but its value should be evaluated for a reference state where this is not true.

3. The second law of thermodynamics

Together with the previous equation, the entropy equation multiplied by T_∞ in its integral form (corresponding to the second law of thermodynamics) is considered:

$$-T_\infty \int_{\partial\mathcal{V}} \rho\delta s(\mathbf{V}' - \mathbf{s_e}') \cdot \mathbf{n}' \,\mathrm{d}S - \int_{\partial\mathcal{V}} \frac{T_\infty}{T}\mathbf{q}' \cdot \mathbf{n}' \,\mathrm{d}S + \int_{\mathcal{V}} \frac{T_\infty}{T^2} k(\nabla T)'^2 \,\mathrm{d}\mathcal{V} + \int_{\mathcal{V}} \frac{T_\infty}{T}\phi' \,\mathrm{d}\mathcal{V} + \int_{\tilde{S}_w} [\![\frac{T_\infty}{T}\mathbf{q}' + T_\infty \rho\delta s(\mathbf{V}' - \mathbf{s_e}')]\!] \cdot \tilde{\mathbf{n}}' \,\mathrm{d}S = 0 \quad (7)$$

where $\phi' = (\overline{\overline{\tau}}' \cdot \nabla') \cdot \mathbf{V}'$ is the dissipation rate per unit volume corresponding to viscous phenomena inside the control volume, and $\mathbf{q}' = -k(\nabla T)'$ corresponds to the Fourier law.

4. Exergy balance equation

The exergy concept is defined as the maximum theoretically recoverable work with respect to a reference state. When considering a perfect gas at rest and neglecting the gravitational potential energy, the specific exergy can be defined as:

$$\epsilon = \delta E + p_\infty \delta\left(\frac{1}{\rho}\right) - T_\infty \delta s \quad (8)$$

When considering a flowing fluid, the flow specific exergy definition is slightly different due to the consideration of the pressure forces driving the flow and the kinetic energy [10]. The specific exergy for a steady flow is expressed mathematically for an open system as:

$$\epsilon_{flow} = \delta H - T_\infty \delta s \quad (9)$$

Both definitions describe the same principle: the valuable energy that can be extracted from a system corresponds to the part of the energy that is not destroyed by irreversible phenomena, which are linked to entropy production. From this, the exergy balance equation can be written in the rotating frame as:

$$\frac{d}{dt}_{\mathbf{s_e}} \int_{\mathcal{V}} \rho\epsilon \,\mathrm{d}\mathcal{V} + \int_{\partial\mathcal{V}} \rho\epsilon(\mathbf{V}' - \mathbf{s_e}') \cdot \mathbf{n}' \,\mathrm{d}S = \frac{d}{dt}_{\mathbf{s_e}} \int_{\mathcal{V}} \rho(\delta E + p_\infty \delta\left(\frac{1}{\rho}\right) - T_\infty \delta s) \,\mathrm{d}\mathcal{V} + \int_{\partial\mathcal{V}} \rho(\delta E + p_\infty \delta\left(\frac{1}{\rho}\right) - T_\infty \delta s)(\mathbf{V}' - \mathbf{s_e}') \cdot \mathbf{n}' \,\mathrm{d}S \quad (10)$$

Which can be simplified in the steady case as:

$$\int_{\partial\mathcal{V}} \rho\epsilon(\mathbf{V}' - \mathbf{s_e}') \cdot \mathbf{n}' \,\mathrm{d}S = \int_{\partial\mathcal{V}} \rho(\delta E + p_\infty \delta\left(\frac{1}{\rho}\right) - T_\infty \delta s)(\mathbf{V}' - \mathbf{s_e}') \cdot \mathbf{n}' \,\mathrm{d}S \quad (11)$$

5. Final steady exergy balance in its absolute velocity, relative frame form

By injecting Eqs. (3) and (7) into Eq. (11), and after several mathematical manipulations, the steady exergy balance for rotating frames in its most general form is obtained:

$$\dot{\mathcal{E}}'_q + W\dot{\Omega}' = W\dot{\Gamma}' + \dot{\mathcal{E}}'_m + \dot{\mathcal{E}}'_{th} + \dot{\mathcal{A}}'_\phi + \dot{\mathcal{A}}'_{\nabla T} + \dot{\mathcal{A}}'_w + \tau'_O + \tau'_{xO} - \dot{E}'_{qO} \quad (12)$$

where several new terms appear:

- $\dot{\mathcal{E}}'_q := -\int_{S_b}(1 - \frac{T_\infty}{T})\mathbf{q}' \cdot \mathbf{n}' \,\mathrm{d}S$ is the rate of exergy supplied by thermal conduction through non-adiabatic walls on S_b. The sum of this term and $W\dot{\Omega}'$ corresponds to the total rate of exergy supplied to the system.

- $\dot{\mathcal{E}}'_m := \underbrace{\int_{S_O} \frac{1}{2}\rho u'^2(\mathbf{V}' - \mathbf{s_e}') \cdot \mathbf{n}' \, \mathrm{d}S}_{\dot{E}'_u} + \underbrace{\int_{S_O} \frac{1}{2}\rho(v'^2 + w'^2)(\mathbf{V}' - \mathbf{s_e}') \cdot \mathbf{n}' \, \mathrm{d}S}_{\dot{E}'_{vw}} + \underbrace{\int_{S_O} (p - p_\infty)(\mathbf{V}' - \mathbf{V}'_\infty) \cdot \mathbf{n}' \, \mathrm{d}S}_{\dot{E}'_p}$ is the mechanical exergy wasted as it leaves the control volume without being used. It is composed of three terms which correspond respectively to the longitudinal kinetic perturbation energy associated to wakes or jets, the transversal kinetic perturbation energy mainly associated to vortices and the boundary pressure work linked to these perturbations. For either a deceleration or an acceleration of the fluid, the first and second terms will be positive. Thus, any velocity perturbation (positive or negative) leads to a creation of exergy which can be potentially transformed into useful work.

- $\dot{\mathcal{E}}'_{th} := \int_{S_O} \rho\delta e(\mathbf{V}' - \mathbf{s_e}') \cdot \mathbf{n}' \, \mathrm{d}S + \int_{S_O} p_\infty(\mathbf{V}' - \mathbf{s_e}') \cdot \mathbf{n}' \, \mathrm{d}S - T_\infty \int_{S_O} \rho\delta s(\mathbf{V}' - \mathbf{s_e}') \cdot \mathbf{n}' \, \mathrm{d}S$ is the thermocompressible exergy wasted. The three terms composing it correspond respectively to the thermal energy outflow, the isobaric boundary pressure work and the total anergy outflow. This term highlights the fact that, contrary to mechanical exergy which can theoretically be fully recovered, only a part of the thermal energy available can be converted to useful work.

- $\dot{\mathcal{A}}'_\phi := \int_{\mathcal{V}} \frac{T_\infty}{T}\phi' \, \mathrm{d}\mathcal{V}$ corresponds to the anergy generation (i.e. the irreversible destruction of exergy) due to viscous phenomena appearing in the flow. It corresponds to a process converting mechanical energy into thermal energy in order to smooth the velocity field and will be reffered to as the viscous anergy, which is always positive.

- $\dot{\mathcal{A}}'_{\nabla T} := \int_{\mathcal{V}} \frac{T_\infty}{T^2} k(\nabla T)'^2 \, \mathrm{d}\mathcal{V}$ is the anergy generation due to the thermal mixing that uniformizes the temperature field in the control volume while the system goes back to a thermal equilibrium state. Again, this term will always be positive as it represents the destruction of exergy inside the control volume through an irreversible process.

- $\dot{\mathcal{A}}'_w := T_\infty \int_{\tilde{S}_w} [\![\frac{1}{T}\mathbf{q}' + \rho\delta s(\mathbf{V}' - \mathbf{s_e}')]\!] \cdot \tilde{\mathbf{n}}' \, \mathrm{d}S$ corresponds to the anergy generation due to the presence of discontinuous shockwaves in the flow.

- $\tau'_O := -\int_{S_O} (\overline{\overline{\tau}}' \cdot \mathbf{V}') \cdot \mathbf{n}' \, \mathrm{d}S$. This term is the rate of work of the viscous force on the outer boundary.

- $\tau'_{xO} := \int_{S_O} (\overline{\overline{\tau}}' \cdot \mathbf{V}'_\infty) \cdot \mathbf{n}' \, \mathrm{d}S$. This term can be usually neglected in the momentum equation at distances greater than one body length downstream of the configuration.

- $\dot{E}'_{qO} := -\int_{S_O} (1 - \frac{T_\infty}{T})\mathbf{q}' \cdot \mathbf{n}' \, \mathrm{d}S$. This term corresponds to the thermal exergy outflow associated with heat conduction across the outer boundary of the control volume.

IV. Numerical application: HAD-1 propeller case

A. Presentation of the case

The HAD-1 case geometry and mesh considered in this study are shown in Fig. 2. It corresponds to a 3-blade propeller in an external flow field with a spinner and a cylinder extending downstream up to the limit of the computational domain. It was designed at ONERA within the European project MADELEINE [11] as a reference case for aerodynamics/aeroacoustics investigations. The blade geometry was designed and studied previously at ONERA [12] [13] to evaluate body-force models. A multiblock structured mesh with around 10.1 million points is used for the numerical computation. It is noted that this corresponds to an "industrial" grid, in the sense that the grid topology and properties follow common standard practices on aerodynamic performance prediction and were not specifically adjusted for the sake of the exergy analyses in this work. The boundary condition applied at all the walls is a no-slip condition, i.e. the flow is viscous near the walls.

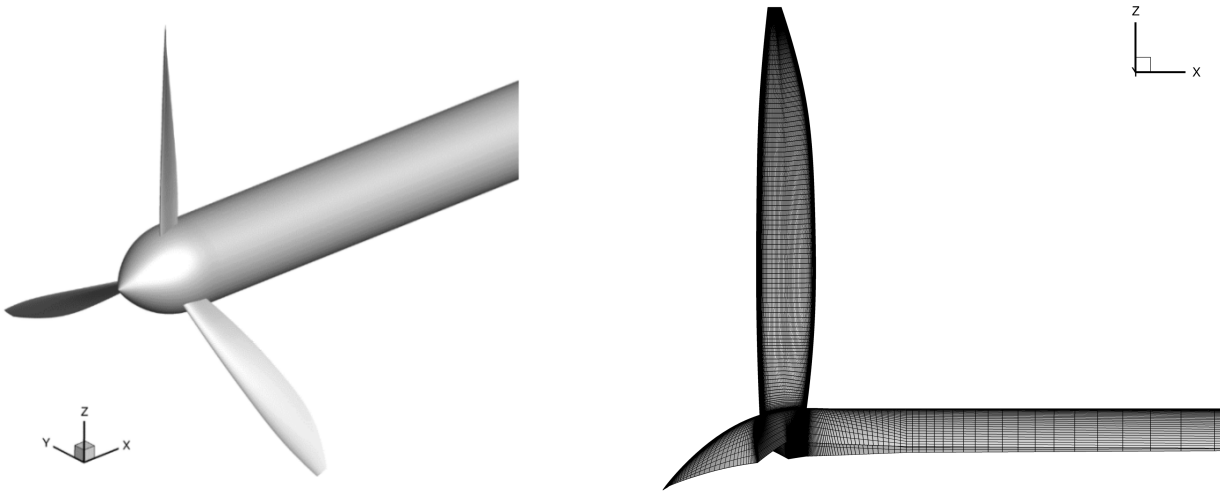

Fig. 2 HAD-1 propeller geometry (left) and side view of the mesh used (right).

The numerical computation that is post-processed with FFX was carried out with the ONERA-Airbus-SAFRAN CFD solver elsA [14], on a 120-degree azimuthal section with periodic boundary conditions. In Fig. 3, iso-surfaces of Q-criterion colored with the relative Mach using the physical fields computed in elsA are shown. The details of the reference state used in the computation (which is the same as the one used for the exergy definition) and the simulation parameters are presented in Table 1.

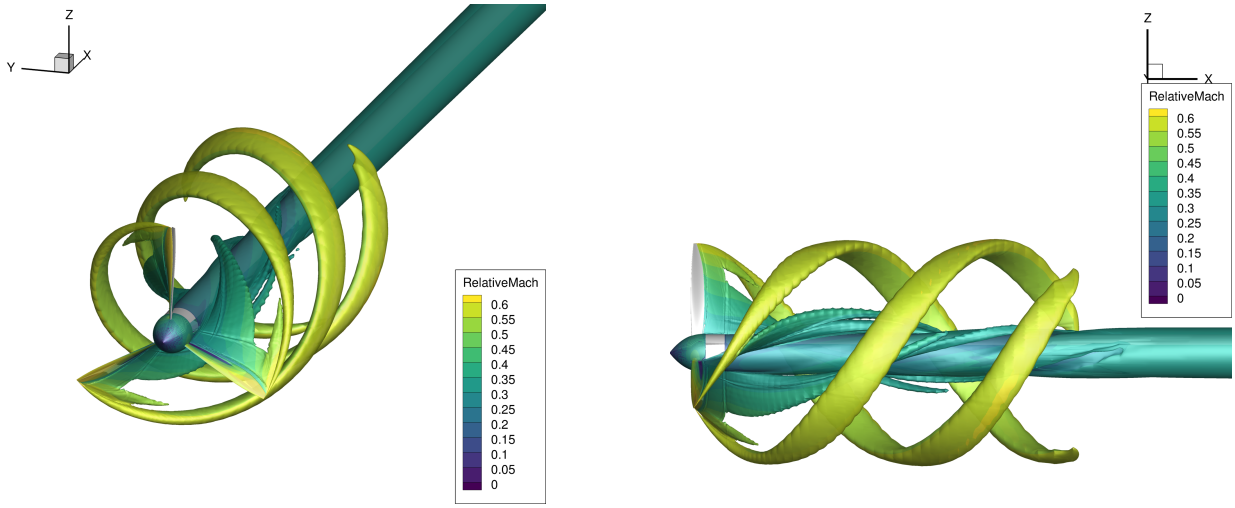

Fig. 3 HAD-1 iso-surface of the Q-criterion colored by the relative Mach number in perspective (left) and side (right) view at operating conditions as detailed in Table 1.

Type of calculation	RANS
Turbulence model	Spalart-Allmaras
Angle of Attack	0.0°
Sideslip Angle	0.0°
Velocity formulation	Absolute
Reference frame	Relative
R_p	0.8m
Re_∞	7. 10^6
M_∞	0.3
ρ_∞	1.225 kg.m^{-3}
T_∞	288.16 K
ω	212.6 rad.s^{-1}

Table 1 Parameters of the CFD computation.

The computational domain extends in the x-direction between $x_{min} = -11.0m$ and $x_{max} = 18.9m$. The propeller, consisting of a spinner and three blades, is situated between the coordinates $x = -0.2m$ and $x = 0.2m$, with the fixed cylinder extending downstream up to the end of the computational domain. During the post-processing with FFX, several numerical operations are ensured in coupling with the free open-source set of python modules for pre- and post-processing of CFD computations named Cassiopée and developed at ONERA [15].

B. Preliminary considerations about the results

As the walls in the HAD-1 case computation are all adiabatic with a no-slip boundary condition, and since there is no shockwave appearing under these flight conditions, $\dot{\mathcal{E}}'_q = 0$ and $\dot{\mathcal{A}}'_w = 0$. Furthermore, as the case of application is one of external aerodynamics that does not involve a significant exchange of heat through its boundaries, and as their negligible values were confirmed numerically, the terms τ'_O, τ'_{xO} and $\dot{E}'_{qO}$ are also neglected in this case. However, it is important to notice that this might not remain possible when studying internal flows, like in the case of a compressor for example. Nevertheless, in this case, Eq. (12) becomes:

$$W\dot{\Omega}' = W\dot{\Gamma}' + \dot{\mathcal{E}}'_m + \dot{\mathcal{E}}'_{th} + \dot{\mathcal{A}}'_\phi + \dot{\mathcal{A}}'_{\nabla T} \tag{13}$$

All the quantities of the exergy balance are normalized with the P_{ref} coefficient:

$$P_{ref} = 0.5\rho_\infty S_{ref} V_\infty'^3 \tag{14}$$

So that the normalized coefficient for the different exergy terms are (taking the viscous anergy $\dot{\mathcal{A}}'_\phi$ as an example):

$$C_{\dot{\mathcal{A}}'_\phi} = \frac{\dot{\mathcal{A}}'_\phi}{P_{ref}} \tag{15}$$

and their non-dimensional values will be given in power counts (pc).
Two figures of merit are also defined in order to characterize the propeller's efficiency in the exergy framework, and computed with FFX. The first one is:

$$\psi_p = \frac{C_{W\dot{\Gamma}'}}{C_{W\dot{\Omega}'}} \tag{16}$$

which will be referred to as the effective propulsive efficiency, i.e. the part of the exergy provided by the propeller that is actually used by the body to maintain its axial mechanical equilibrium. A second quantity can be introduced:

$$\psi_{p_m} = \frac{C_{W\dot{\Gamma}'} + C_{\dot{\mathcal{E}}'_m} + C_{\dot{\mathcal{E}}'_{th}}}{C_{W\dot{\Omega}'}} \tag{17}$$

which is the theoretical maximum propulsive efficiency that could be obtained in the domain, the rest of it being exergy destroyed by irreversible phenomena. This term should theoretically always be higher than ψ_p and can never be equal

to one in the case of Navier-Stokes simulations. This is because irreversibilities present in the flow lead to anergy generation, corresponding to exergy destruction, and prevent the possibility to completely transform the exergy provided by the propeller into useful work.

C. Numerical results obtained

1. Evolution of exergy coefficients at different downsteam Trefftz planes positions

In this section, the exergy balance is computed for a series of downstream limits of the control volume with the x-coordinate for each Trefftz plane noted x_{TP}. The values selected for x_{TP} will not be higher than $x_{TP_{max}} = 5.0m$ in order to avoid the regions where the mesh becomes too coarse to accurately resolve the flow field and to be able to perform a fine exergy analysis. These values range from $x_{TP_{min}} = -5.0m$ up to $x_{TP_{max}} = 5.0m$ with a step of 0.5m between them. The station situated at $x_{TP} = 0.0m$ is not plotted nor investigated as the downstream limit of the control volume intersects the propeller blades, making the physical interpretation of the exergy balance non-straightforward.

The values of the exergy provided by the propeller $W\dot{\Omega}'$ and the exergy consumed to maintain a steady state $W\dot{\Gamma}'$, together with its effective and maximal attainable efficiencies are shown in Fig. 4.

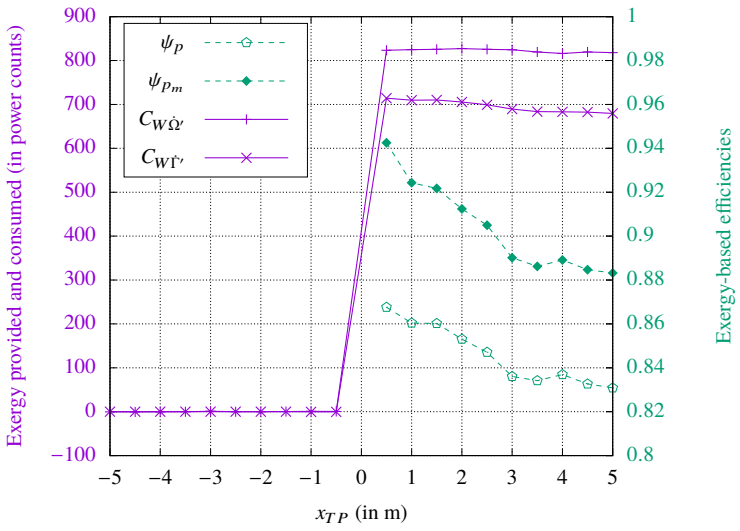

Fig. 4 Exergy provided and consumed by the system and efficiencies as functions of x_{TP}.

Fig. 4 shows that the term $C_{W\dot{\Omega}'}$ is equal to zero up to $x_{TP} = -0.5m$. This is because there is no exergy transferred from the propeller to the fluid up to the beginning of the spinner. It then reaches a value of approximately 823 pc, with a few variations which are due to the effect of the cylinder and some numerical noise. As soon as the control volume reaches the propeller, the curve for $C_{W\dot{\Gamma}'}$ follows the curve of $C_{W\dot{\Omega}'}$ up to 714 pc before starting to drop. This shows that not all the exergy supplied by the propeller is consumed by the system, but only part of it can be potentially used, explaining why this curve does not reach the same level as $C_{W\dot{\Omega}'}$. It then decreases due to the presence of the infinite cylinder downstream: indeed, viscous drag increases when a bigger part of the cylinder is included as the control volume extends downstream, which leads to a degraded performance of the global system.

The values for ψ_p and ψ_{p_m} are plotted for $x_{TP} \geq 0.5m$: indeed, the efficiency of the propeller has a clear interpretation only when the propeller is actually included in the control volume. In Fig. 4, as a longer section of the cylinder is included in the control volume, the maximum and effective efficiencies decrease. This is consistent with the evolutions of $C_{W\dot{\Omega}'}$ and $C_{W\dot{\Gamma}'}$ which show that the performance is degraded with the increase of x_{TP}. But the exergy balance gives a supplementary information here, which is that there is room for improvement in this configuration to reach the maximum propulsive efficiency by attempting to recover the components of exergy outflow. For example, at $x_{TP} = 2m$, this efficiency could be increased from 85.3% up to a maximal efficiency of 91.2% by a reduction of exergy outflow from the control volume, assuming that this modification could be achieved without affecting the anergy generation within the control volume. Both these efficiency curves slopes are modified beyond $x_{TP} = 3.0m$, this is

because downstream of this plane the cell size increases and the mesh becomes more coarse leading to higher numerical imprecision.

The exergy outflow, i.e.wasted, and the anergy generated are then plotted in Fig. 5:

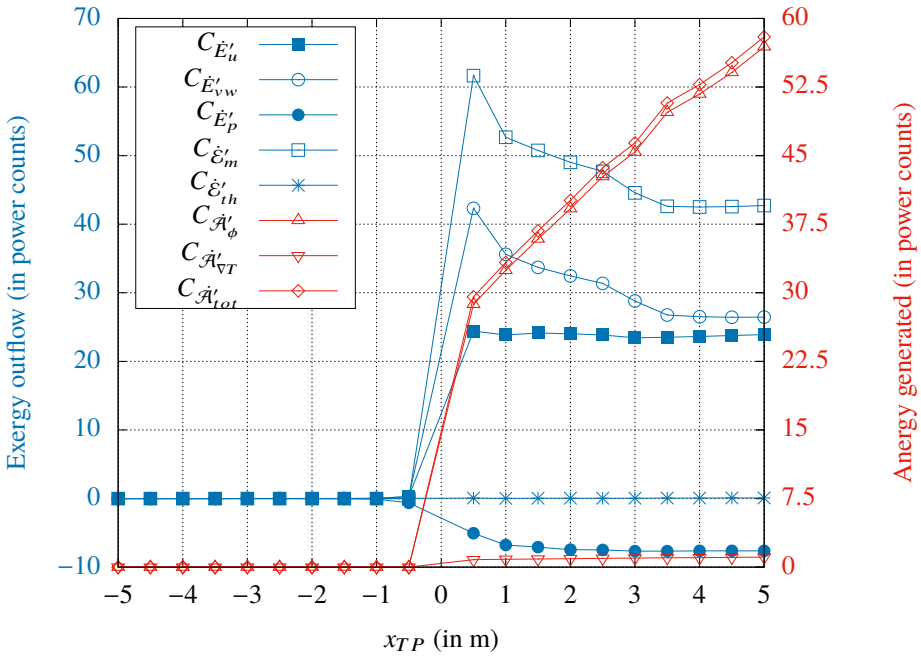

Fig. 5 Components of exergy outflow and anergy generated as function of x_{TP}

All components are null before the propeller is included inside the control volume. Then, large variations can be observed when the Trefftz plane is moved from upstream to downstream of the propeller. In the vicinity of the propeller, the fluid particles are accelerated, leading to an increase in $C_{\dot{E}'_u}$ and $C_{\dot{E}'_{vw}}$ and a decrease in $C_{\dot{E}'_p}$, the sum of these three terms giving an increase in mechanical exergy. Further downstream, all exergy outflow components start to decrease: the exergy outflow is reduced as exergy is destroyed by irreversible effects. Correspondingly, the anergy generated increases when pushing x_{TP} downstream. The main irreversible effect appearing here is the dissipation by viscous effects of the flow exergy: $C_{\dot{\mathcal{A}}'_\phi}$ is much higher than $C_{\dot{\mathcal{A}}'_{\nabla T}}$. This and the very low values for the thermal exergy $C_{\dot{\mathcal{E}}'_{th}}$ highlight that temperature variations and thermal exchanges are secondary compared to viscous effects and mechanical exergy for this configuration at this reference state (the Mach number is low and there is no shockwave appearing, plus all the walls are adiabatic). The values for the coefficients of the exergy balance with four different Trefftz planes limiting the control volume are shown in Table 2, with the residual coming from the imbalance between the two sides of the exergy balance equation. The Exergy-Waste Coefficient (EWC), introduced by Arntz [5] as:

$$EWC = \frac{\dot{\mathcal{E}}_m + \dot{\mathcal{E}}_{th}}{\dot{\mathcal{E}}_m + \dot{\mathcal{E}}_{th} + \dot{\mathcal{A}}_{tot}} \tag{18}$$

is also computed using the quantities expressed in the relative frame.

x_{TP} (in m)	$\frac{x_{TP}}{R_p}$	$C_{W\dot{\Omega}'}$	$C_{W\dot{\Gamma}'}$	$C_{\dot{E}'_u}$	$C_{\dot{E}'_{vw}}$	$C_{\dot{E}'_p}$	$C_{\dot{\mathcal{E}}'_m}$	$C_{\dot{\mathcal{E}}'_{th}}$	$C_{\dot{\mathcal{A}}'_\phi}$	$C_{\dot{\mathcal{A}}'_{\nabla T}}$	Residual	EWC
0.2	0.25	824.84	719.32	23.39	49.27	-4.07	68.59	0.39	26.23	0.80	9.51	0.72
0.5	0.625	823.38	714.36	24.40	42.32	-5.06	61.66	0.07	28.73	0.82	17.72	0.68
1.0	1.25	824.95	709.79	23.85	35.61	-6.77	52.59	0.04	32.45	0.86	29.13	0.61
2.0	2.5	827.24	705.70	24.02	32.46	-7.45	49.03	0.05	39.19	0.93	32.34	0.55

Table 2 Exergy balance computed for fixed Trefftz planes. All exergy coefficients are expressed in power counts.

When the Trefftz plane is placed further downstream, the residual of the exergy balance increases. This is due to numerical effects, a subject which is further investigated and discussed in Sec. IV.D. Fig. 2 also shows that, the more downstream the Trefftz plane is, the less exergy flows out of the control volume relative to the total anergy generated. This is because exergy is progressively dissipated by irreversible effects (mainly viscous effects) which lead to anergy generation.

2. Analysis of physical phenomena using exergy and anergy contours.

Studying contours of the exergy balance terms allows to describe the physical phenomena taking place in the control volume. To do so, several stations at a fixed x coordinate can be used to view where the different terms of the exergy balance have significant values and to what phenomena they can be related. Three stations are selected at the coordinates $x = 0.2m$, $x = 0.5m$ and $x = 1.0m$, as represented in Fig. 6:

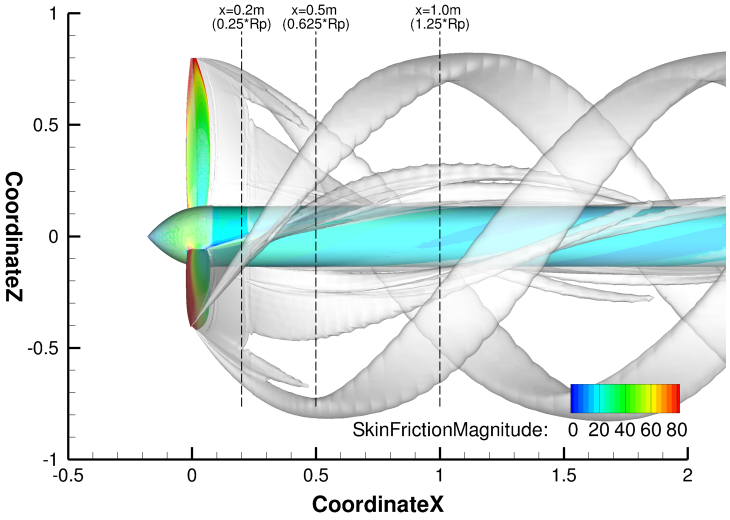

Fig. 6 Side view of the downstream stations at $x = 0.2m$, $x = 0.5m$ and $x = 1.0m$ selected for contour vizualisation.

The contours of exergy outflow are then plotted for these stations, as shown in Figs. 7, 8, 9 and 10. The propeller geometry is superposed to vizualise the blade geometries and positions.

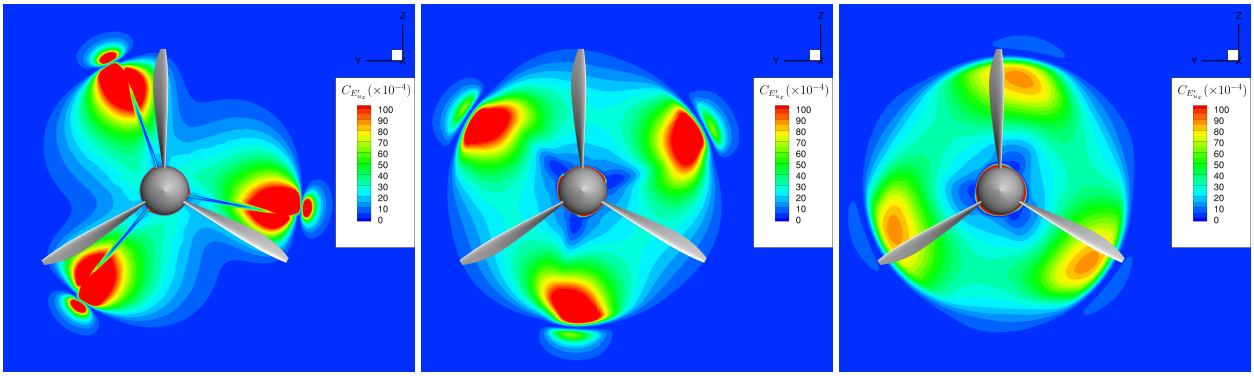

(a) $x = 0.2m$ **(b)** $x = 0.5m$ **(c)** $x = 1.0m$

Fig. 7 Contours of streamwise kinetic perturbation energy at different fixed x coordinates.

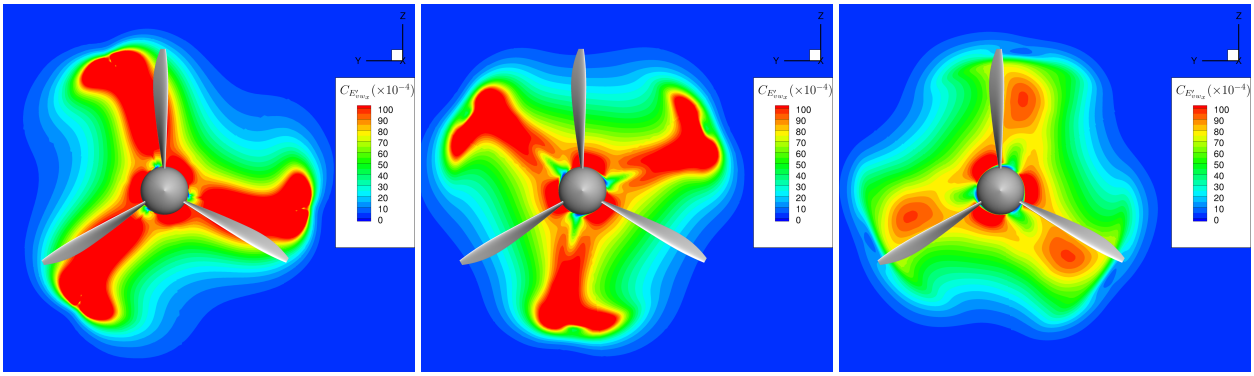

(a) $x = 0.2$ **(b)** $x = 0.5m$ **(c)** $x = 1.0m$

Fig. 8 Contours of transversal kinetic perturbation energy at different fixed x coordinates.

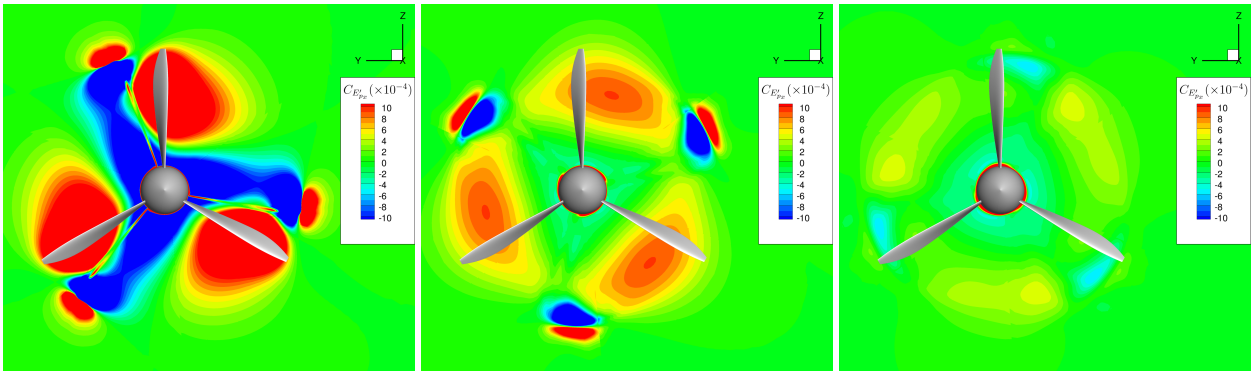

(a) $x = 0.2m$ **(b)** $x = 0.5m$ **(c)** $x = 1.0m$

Fig. 9 Contours of pressure work related to velocity perturbations at different fixed x coordinates.

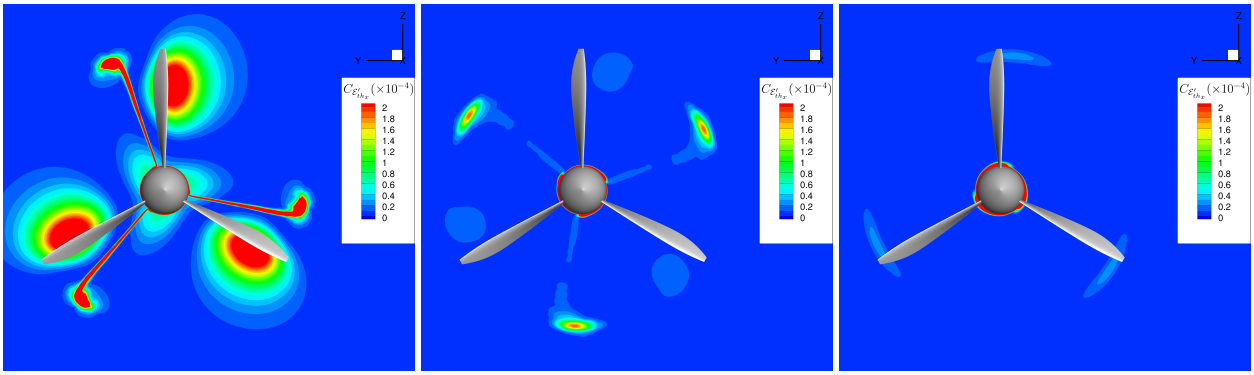

(a) $x = 0.2m$ **(b)** $x = 0.5m$ **(c)** $x = 1.0m$

Fig. 10 Contours of thermocompressible exergy at different fixed x coordinates.

Downstream of the propeller, there is a system of three vortices attached to the propeller wake. Inside these structures, the pressure and velocity are different from their values in the reference state leading to exergy components that are not null. Fig. 7 shows that the flow is accelerated by the propeller, leading to a large region with kinetic energy outflow, which also appears for the transversal perturbation kinetic energy in Fig. 8. The system of vortices also clearly appears with local axial perturbation kinetic energy outflow at the tip of the blade wake, as can be seen in Fig. 7. Both

these exergy components are always positive, highlighting that any kinetic exergy linked to deceleration or acceleration can be potentially used. These structures can also clearly be distinguished from the boundary layer of the cylinder, with a kinetic energy variation in the region close to it. These observations can be confirmed when looking at the pressure-work rate related to these velocity perturbation in Fig. 9. Indeed, tip vortices can clearly be distinguished with the blades' wake, characterised by a decrease of pressure. For this last term, in addition to these structures, a large zone with higher pressure that does not seem to be rotating with the wake of the blades is observed. This can also be seen when looking at thermal exergy contours in Fig. 10, where the rotating wake of the blades can clearly be followed as there is thermal exergy available in this wake and at the center of the tip vortices. On this last figure, the non-rotating zone spotted in Fig. 9 is also present with thermal exergy available. This zone actually corresponds to the high pressure due to flow passing close to the blades of the propeller, and hence stays attached to the blade. This means that this zone is actually rotating at the same velocity as the propeller, making it appear motionless in the rotating frame.

These figures allow to describe the physics of the flow by looking at the components of exergy outflow. But the kinetic energy present inside the vortices and the propeller wake is then progressively dissipated primarily by the viscous forces, as indicated by the increase of viscous anergy generation discussed above (see Fig. 5). The same observation can be made with regard to thermal exergy, which is dissipated primarily through thermal mixing corresponding to an increase of thermal anergy. This can be observed by plotting anergy contours, as shown in Figs. 11 and 12:

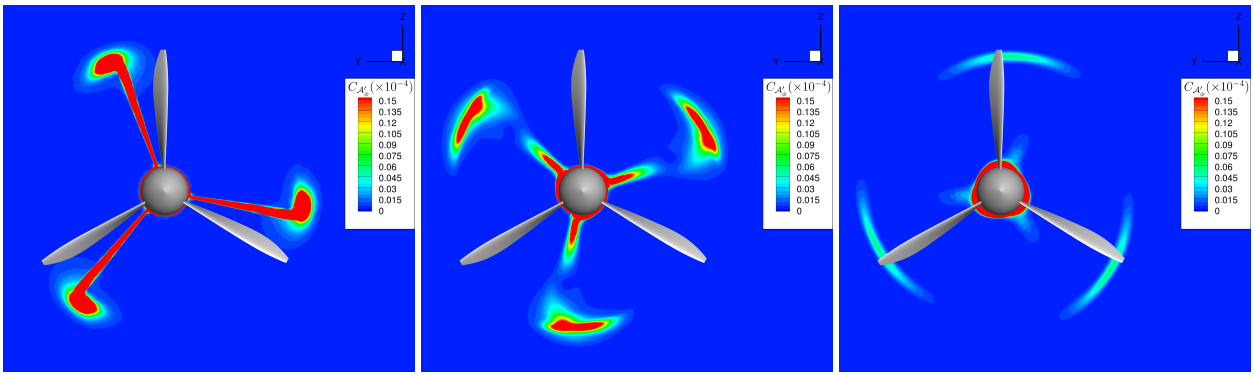

(a) $x = 0.2m$ **(b)** $x = 0.5m$ **(c)** $x = 1.0m$

Fig. 11 Contours of viscous anergy generation at different fixed x coordinates.

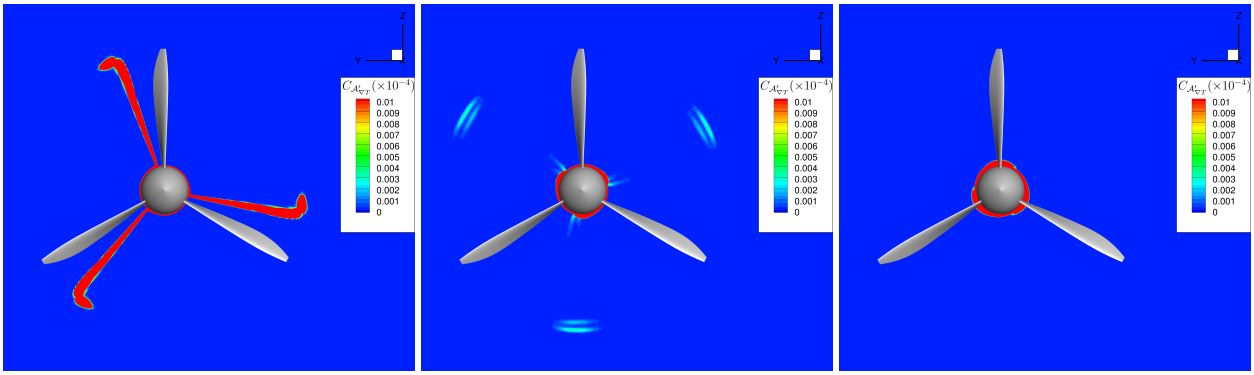

(a) $x = 0.2m$ **(b)** $x = 0.5m$ **(c)** $x = 1.0m$

Fig. 12 Contours of thermal anergy generation at different fixed x coordinates.

These anergy contours allow to confirm that the viscous phenomena are the dominating effects in the propeller's wake. As stated previously, the exergy available in the blades' wake and in the tip vortices is dissipated, leading to regions of anergy production that follow the regions of exergy outflow that were discussed above. The anergy produced in those regions decreases while pushing the station analysed downstream, as the flow evolves towards its reference thermodynamical state. The non-rotating regions of high pressure and thermal exergy are not appearing in anergy

contours, confirming that they are not linked to velocity effects. Finally, part of the dissipation also occurs in the boundary layer of the cylinder for which the anergy generation does not decrease: in this region the flow does not return to its reference state as the cylinder extends up to the end of the control volume. This can also be seen in Fig. 5.

3. Study of the propeller under different freestream flow conditions

Now that the study has been presented for one set of flow conditions, it is possible to perform the same kind of exergy analysis under different ones to evaluate its performance in off-design conditions. To do so, the pitch angle of the propeller remains constant and the control volume is limited at $x_{TP} = 0.2m$ in order to only analyse the rotating parts of the body, i.e. the spinner and the blades. The freestream velocity V_∞ is then modified in order to adjust the propeller advance ratio J, defined as:

$$J = \frac{V_\infty}{2R_p N} \tag{19}$$

where $N = \frac{\omega}{2\pi}$ is the angular velocity expressed in rotations per second.
Then, three different angular velocity values are selected, corresponding to $\omega = 212.6$ rad.$^{-1}$, $\omega_{90\%} = 191$ rad.$^{-1}$ and $\omega_{110\%} = 234.4$ rad.$^{-1}$, i.e. the initial angular velocity to which roughly 10% of its value is added or substracted. For each of these values, several numerical computations are performed with elsA for M_∞ varying between 0.24 and 0.50 with a step of 0.02. The other freestream values are kept constant in order to have this variation corresponding to a V_∞ variation. Then, the exergy-based efficiencies, the corresponding net power consumed and the exergy provided by the propeller are computed and plotted in Fig. 13:

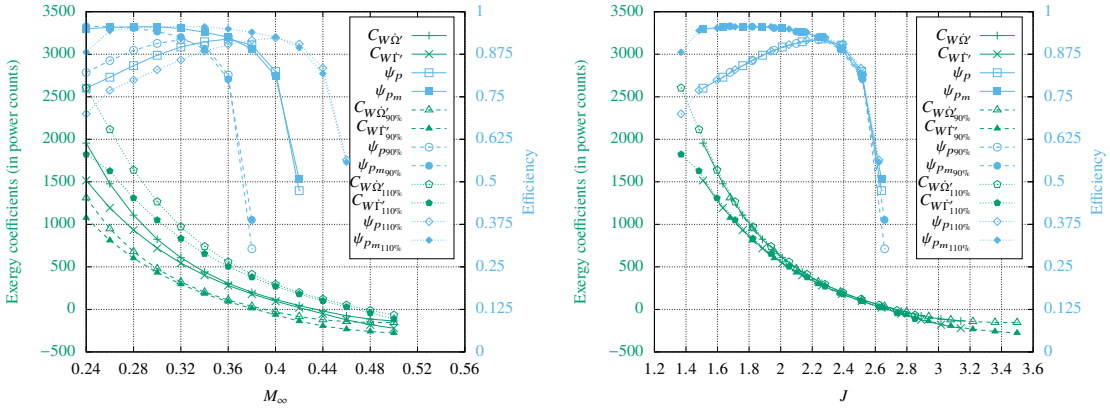

Fig. 13 Exergy-based shaft power, consumed power and efficiencies as functions of M_∞ (left) and of the propeller advance ratio J (right) for $x_{TP} = 0.2m$ with ω (solid lines), $\omega_{90\%}$ (dashed lines) and $\omega_{110\%}$ (dotted lines).

Fig. 13 shows that for all three angular velocities, the more J increases, the less shaft power is available and the less axial mechanical power is obtained. The evolution of ψ_p also shows that the maximum effective efficiency of this propeller with an angular velocity of 212.6 rad.s^{-1} is obtained at a freestream state with $M_\infty = 0.36$ corresponding to $J = 2.26$. Further increasing the freestream Mach number leads to a steep decrease in the propeller efficiency, with no torque converted to thrust obtained for a J value between 2.6 and 2.8. For higher J values, the propeller is no longer producing/providing a propulsive force but instead generates more drag power than thrust power. Modifying the angular velocity and plotting these curves for the same range of M_∞ values allows to translate the global shape of the curve on the left graph of Fig. 13: indeed, the M_∞ value corresponding to the optimal effective efficiency is lower when ω decreases, while it is higher when ω increases. The right graph of Fig. 13 shows that modifying the angular velocity does not change the trend nor the values of the different quantities plotted as all the curves overlap. Thus, whereas changing the angular velocity indeed leads to a change of the optimal freestream velocity in terms of efficiency, this always corresponds to a same optimal value of the advance ratio.

The exergy balance allows to get another information by plotting the evolution of ψ_{p_m}. This quantity gives an estimation of the maximum efficiency that could be theoretically obtained for the different operating regimes. Its behavior is not the same when going below the optimal J and M_∞ than when going above. For example, in the case where $\omega = 212.6$ rad.s^{-1}, while the maximum efficiency that could be theoretically obtained stays almost constant at a

value close to 95% for M_∞ values below 0.32, it then starts dropping to meet the effective efficiency curve at $M_\infty = 0.36$ and follows it very closely in the efficiency drop part when M_∞ keeps increasing. The curve for the maximum efficiency theoretically attainable is also shifted towards higher values of M_∞ when increasing the angular velocity, delaying its sudden decrease towards higher M_∞ values, whereas another performance degradation appears at low M_∞ values for the highest angular velocity studied. Plotting ψ_{p_m} as a function of J again leads to an overlap of the curves for the three different angular velocities investigated. The same trend of a decrease of the maximum attainable efficiency is also observed for J values above 2, with a similar value between ψ_p and ψ_{p_m} obtained for $J = 2.26$ before both quantities decrease significantly. This means that working at operating regimes with J values below the optimal one leads to a decreased effective efficiency due partly to high amounts of wasted exergy, while working above it leads to a steep decrease in efficiency that is mostly due to irreversible destruction of exergy.

For all three angular velocities studied, there are points near J values for which both efficiencies decrease where the effective efficiency is higher than the maximal attainable efficiency. This behavior is not expected according to the definition of these figures of merits and should not be appearing. The reason for this behavior has to be investigated and is currently attributed to potential numerical imprecision issues. Indeed, this happens for higher J values for which both $C_{W\dot{\Gamma}'}$ and $C_{W\dot{\Omega}'}$ have very low values, which could lead to an higher impact of numerical errors.

The physical analysis can be completed by plotting the evolution of the components of the exergy balance for these different operating regimes at one fixed $\omega = 212.6$ rad.s^{-1} value, as shown in Fig. 14.

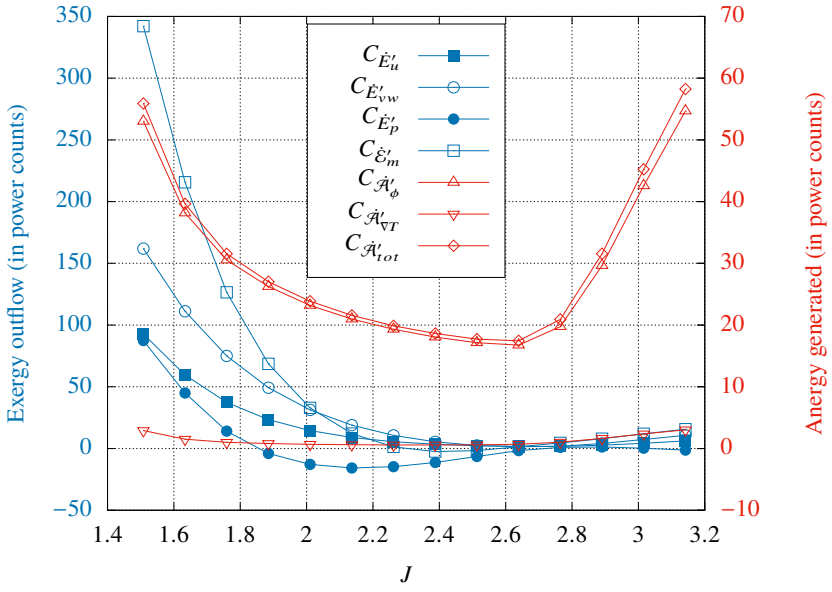

Fig. 14 Exergy outflow and anergy generated as functions of the advance ratio for $\omega = 212.6$ rad.s^{-1} and $x_{TP} = 0.2m$.

It can be seen here that there is a steep decrease both in mechanical exergy outflow and in anergy generation when approaching the optimal operating regime. However, the mechanical exergy outflow decreases much faster than the anergy generation, with an up to 300 power-count decrease between the minimum value of J and the optimal one, while the anergy generation decreases by 35 power counts. It can also be deduced that the optimal operating regime, situated at $J = 2.26$ for this angular velocity, does not correspond to a minimum of exergy destruction (i.e. anergy generation) but rather to a low anergy generation combined with low levels of mechanical exergy outflow. This highlights the importance of using a complete exergy balance formulation to investigate the propeller's performance, instead of an individual component. Furthermore, when the efficiency starts decreasing significantly around $J = 2.39$, the anergy generation shows small variations at its lower peak while the mechanical exergy outflow is close to zero. Then, increasing the J value leads to an increase in total anergy generation again with a steeper slope than the previous decrease while the exergy outflow stays at very low values. This explains why the theoretically attainable efficiency drops alongside with the effective efficiency. In the range of J values where the propeller is not providing thrust anymore as it generates more drag, the exergy outflow stays very low while the total anergy (mainly viscous anergy) increases significantly.

The physical explanation for these exergy terms and efficiency evolutions can be found with a schematic illustration of the velocity triangle for one airfoil section of a propeller blade, as shown in Fig. 15 below where the section is considered as a flat plate:

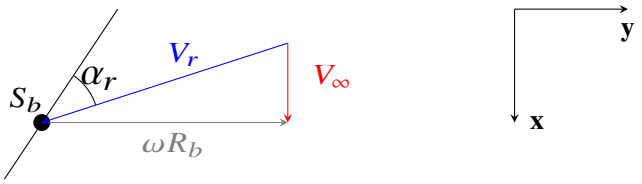

Fig. 15 Blade section situated at a radius R_b represented as a thin plate.

Fig. 15 shows that increasing the reference velocity magnitude V_∞ or decreasing the angular velocity ω leads to a lower local relative angle of attack α_r for the different blade sections. Hence, when V_∞ increases sufficiently, corresponding to an increase of the propeller advance ratio J, the relative angle of attack becomes negative and the propeller starts to slow down the system under study rather than providing a propulsive force. On the contrary, decreasing V_∞ or increasing ω leads to an increase in this angle of attack, which means that for J values that are low enough one could observe a stall phenomenon on different blade sections, which also decreases the efficiency obtained. This phenomenon begins to appear for the angular velocity $\omega_{110\%}$ at the lowest J value investigated, where ψ_{p_m} starts decreasing alongside ψ_p. This evolution of the angle of attack can also be observed by plotting pressure contours at a fixed radius of $R = 0.75$ m for example, as shown in Fig. 16. Streamtraces based on the relative velocity components also highlight the presence of a recirculation bubble appearing when the propeller switches to a brake mode, i.e. for higher values of M_∞.

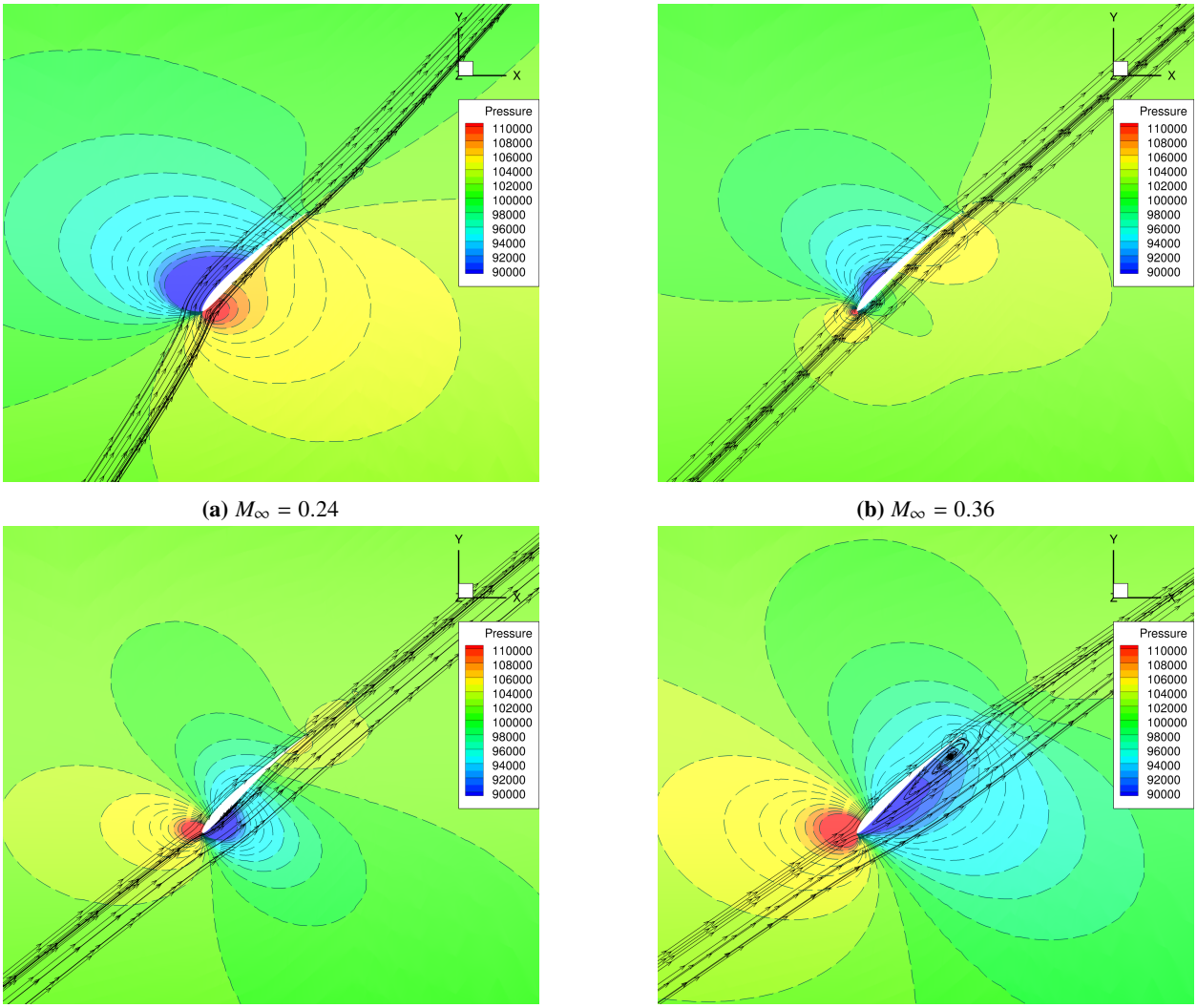

(a) $M_\infty = 0.24$ **(b)** $M_\infty = 0.36$

(c) $M_\infty = 0.44$ **(d)** $M_\infty = 0.50$

Fig. 16 Pressure contours and streamlines based on relative velocity around one blade cut situated at a fixed radius of R = 0.75m for different freestream Mach numbers at a fixed ω = 212.6 rad.s^{-1}.

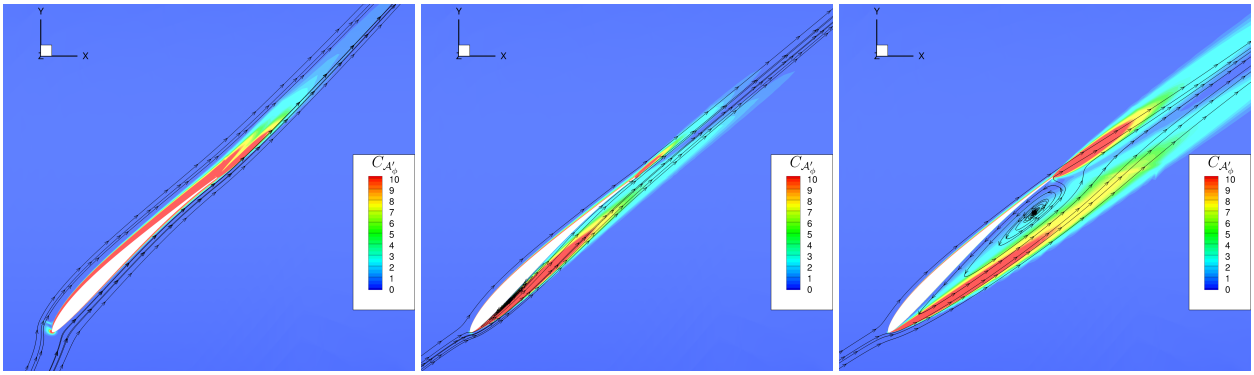

Fig. 17 Viscous anergy contours for $M_\infty = 0.24$ (left), $M_\infty = 0.44$ (middle) and $M_\infty = 0.50$ (right) with $\omega = 212.6$ rad.s^{-1} at a fixed radius of R = 0.75m.

In addition to these pressure contours, viscous anergy contours are also plotted for this blade cut in Fig. 17. When the local relative angle of attack is positive, the viscous anergy generation is mostly located on the upper surface and in the wake of the airfoil section. When it becomes negative, corresponding to a higher freestream Mach number, the viscous dissipation mainly occurs on the lower surface and in the wake of the blade section, with a region of anergy generation close to the trailing edge that gets more important. The presence of a recirculating bubble is also detected with a region of low anergy generation situated close to the airfoil lower surface. Finally, iso-surfaces of viscous anergy for these three cases are shown in Figs. 18 and 19.

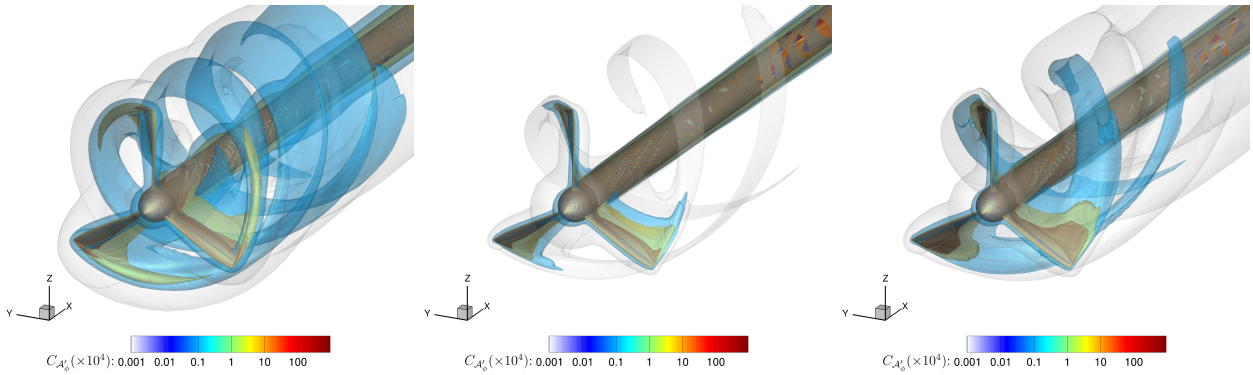

Fig. 18 Iso-surfaces of viscous anergy for M_∞ = 0.24 (left), M_∞ = 0.44 (middle) and M_∞ = 0.50 (right) with ω = 212.6 rad.s^{-1} in perspective view.

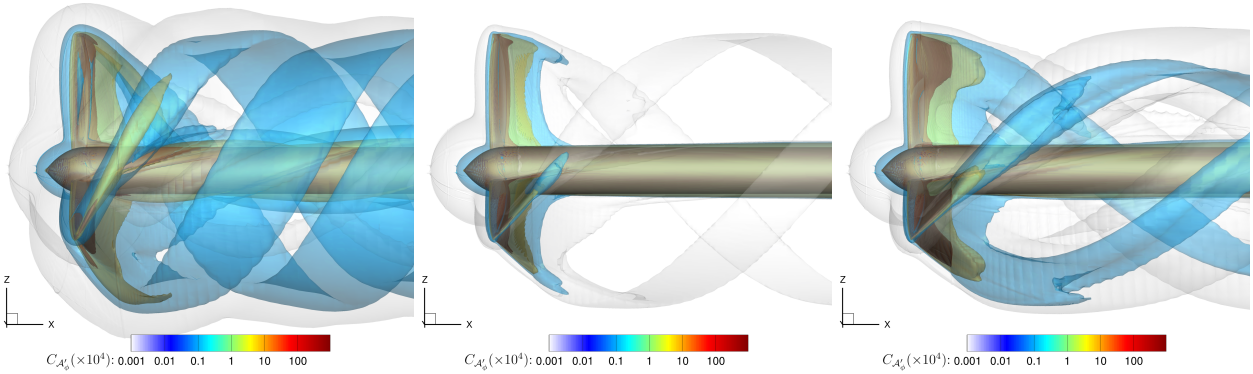

Fig. 19 Iso-surfaces of viscous anergy for M_∞ = 0.24 (left), M_∞ = 0.44 (middle) and M_∞ = 0.50 (right) with ω = 212.6 rad.s^{-1} in side view.

The vizualization of viscous anergy iso-surfaces in Figs. 18 and 19 is in agreement with the analyses made in Fig. 14. The case with a freestream Mach number equal to 0.44 is linked to lower levels of anergy generation in the wake of the blades, with viscous anergy mainly generated close to the propeller. For the two other freestream Mach numbers, the anergy generated stays significant in the vortices downstream of the propeller, explaining the high level of anergy generation observed in Fig. 14. However, there is a difference between the viscous anergy iso-surfaces plotted for M_∞ = 0.24 and M_∞ = 0.50. While both cases correspond to high levels of anergy generation, the iso-surfaces do not have the same geometrical form. In the case corresponding to the lower J value, the viscous anergy is mainly generated close to the propeller and in the propeller wake, with corresponding iso-surfaces following the vortices. The significant dissipation appearing in the vortex structures is due to high levels of mechanical exergy outflow inside it. In the case corresponding to the higher J value, while non-negligible levels of anergy generation are also situated inside the wake vortices, the main part of it is situated close to the propeller. More specifically, a large structure of anergy generation can be observed close to the propeller. Hence, in this case, a lower level of mechanical exergy outflow is also dissipated in the wake vortices, but the main dissipation seems to be located close to the propeller due to the local relative angle of attack being negative, in agreement with that was observed in Fig. 17.

D. Precision analysis

1. Numerical indicators for post-processing precision

Now that the different results have been presented, the precision of the exergy balance should also be discussed. To do so, we will study the initial operating regime that was studied in section IV.C.1, i.e. $\omega = 212.6$ rad.s^{-1} and $M_\infty = 0.3$. If the estimation of the different terms of the exergy balance were perfect, the residual of Eq. (13) should be exactly zero. However, due to numerical dissipation linked to the turbulence model, the mesh and the numerical approximation of the different terms, this balance is not always respected at the discrete level. It is even more so in the case of an industrial grid, where mesh quality may be locally degraded in order to accommodate complex technological details in the geometry or to reduce the number of points in flow regions that are not of primary interest.

Recently, numerical precision indicators have been investigated for this reason at ONERA. These consist in evaluating the error that is made in the energy conservation and the error made on the entropy equation at the discrete level, among others. Two such indicators are respectively denoted as H^* and S^*, with the corresponding expressions in the rotating reference frame formulation applied to the current propeller case:

$$H^* = \int_{\partial\mathcal{V}} (\rho\delta E(\mathbf{V}' - \mathbf{s_e}') + p\mathbf{V}') \cdot \mathbf{n}' \, \mathrm{d}S \tag{20}$$

$$S^* = -T_\infty \int_{\partial\mathcal{V}} \rho\delta s(\mathbf{V}' - \mathbf{s_e}') \cdot \mathbf{n}' \, \mathrm{d}S + \int_{\mathcal{V}} \frac{T_\infty}{T^2} k(\nabla T)'^2 \, \mathrm{d}\mathcal{V} + \int_{\mathcal{V}} \frac{T_\infty}{T} \phi' \, \mathrm{d}\mathcal{V} \tag{21}$$

H^* allows to detect differences that may be associated to grid quality, insufficient convergence or numerical oscillations. S^* is dominated by entropy generation through numerical dissipation. Naturally, this becomes significant downstream of aerodynamic bodies due to the dissipation of wakes and vortices by the numerical discretization and the turbulence model. The discrete error of the exergy balance equation can be expressed as $E^* = H^* - S^*$. As such, the numerically adapted exergy balance takes the following form:

$$W\dot{\Omega}' = \underbrace{W\dot{\Gamma}' + \dot{\mathcal{E}}'_m + \dot{\mathcal{E}}'_{th} + \dot{\mathcal{A}}'_\phi + \dot{\mathcal{A}}'_{\nabla T} - E^*}_{RHSc} \tag{22}$$

While this balance is respected, it is stressed that it is not trivial to rigorously distinguish between the physical and the numerical effects in the total difference contained in E^*. For this reason, H^* and S^* do not correspond to a correction but rather to an estimation of numerical errors in the analysis. Specific strategies have been developed in order to quantify and isolate these numerical errors, in particular the *purely* numerical anergy generation (also called spurious anergy) [6].

It is then interesting to plot the evolution of both H^* and S^* on one side, and of the RHS, LHS (right-hand side and left-hand side respectively) and of RHSc on the other side to verify that the balance is respected:

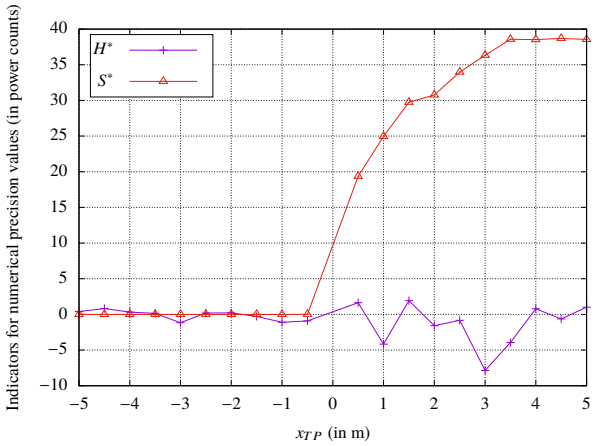

(a) Evolution of H^* and S^* as functions of x_{TP}.

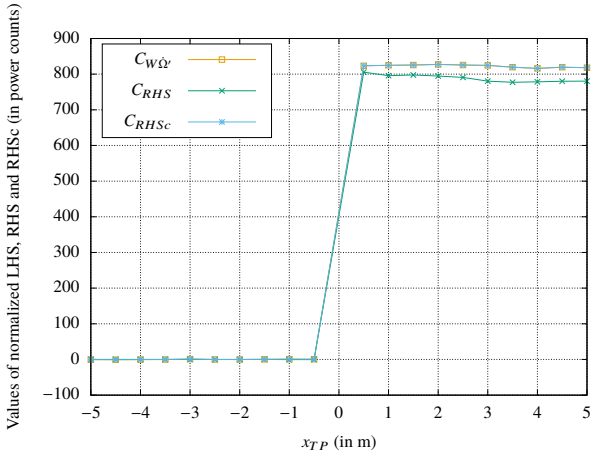

(b) Evolution of the LHS, RHS and RHSc of the exergy balance as a function of x_{TP}.

Fig. 20 Numerical error quantification for various downstream limits of the control volume.

Fig. 20 shows that the inclusion of the E^* term as in Eq. (22) leads to a balanced equation. H^* varies when moving the Trefftz plane downstream, but its absolute values remain within 5 power counts close to the propeller blade. Beyond roughly 2.5 meters, the grid is coarsened so the variations become more important. On the other hand, S^* is not significant until the propeller is included inside the control volume. This is a result of numerical dissipation (numerical discretization and/or turbulence model) which naturally becomes even more significant further downstream.

2. Precision of $W\dot{\Omega}'$ and $W\dot{\Gamma}'$.

Since $W\dot{\Omega}'$ represents the power transferred to the fluid through the torque available at the shaft and $W\dot{\Gamma}'$ represents the part of it that is effectively converted into a power corresponding to the overall force projected on the x-axis (effective thrust in this case), the values obtained for these coefficients are compared with the values obtained from a near-field integration done by elsA. This can also be compared to the near-field values obtained using *ffd01* [1], another post-processing tool developed at ONERA allowing to perform a far-field drag breakdown and which was also adapted in the case of a rotating reference frame [16] [17]. The absolute values obtained for the near-field (NF) elsA and *ffd01* computations for the axial force C_{F_X} and torque power C_{T_X} are shown in Table 3. These are to be respectively compared with the near-field and far-field (FF) values obtained with FFX for $C_{W\dot{\Gamma}'}$ and $C_{W\dot{\Omega}'}$ that are also shown in Table 3. These absolute values and relative errors with the elsA values taken as reference are computed for $x_{TP} = 0.2$m.

Software	elsA		*ffd01*		FFX			
Approach	NF		NF		NF		FF	
Variable	C_{F_X}	C_{T_X}	C_{F_X}	C_{T_X}	$C_{W\dot{\Gamma}'}$	$C_{W\dot{\Omega}'}$	$C_{W\dot{\Gamma}'}$	$C_{W\dot{\Omega}'}$
Absolute value (in counts)	733.05	847.08	734.15	846.29	734.47	846.36	719.32	824.84
Error relative to elsA NF	0%	0%	0.15%	-0.09%	0.19%	-0.08%	-1.87%	-2.63%

Table 3 Coefficient comparison for the partial domain analysis (x_{TP} = 0.2m).

Table 3 shows that the near-field values computed with *ffd01* are in very close agreement with the values computed with elsA. Part of the differences in values computed with these tools can be atributed to different methods used to reconstruct viscous fluxes on wall boundaries. The values obtained with near-field computations performed by FFX show that $C_{W\dot{\Omega}'}$ and $C_{W\dot{\Gamma}'}$ are also in good agreement with these results. On the other hand, the far-field values obtained are different to the ones obtained by the near-field integration with an error closer to 2 and 3 % for the resulting force and shaft power. The higher error on $C_{W\dot{\Omega}'}$ and the difference between its value when computed with near-field and far-field methods tend to show that an error on the entrainment velocity could be the reason for this difference, as it is a term that depends highly on it. Indeed, another source of inaccuracy may come from the evaluation of $\mathbf{s_e}'$. The values used for the post-processing are cell-centered, which is not a cause for any issue in values that do not depend on the mesh coordinates. However, $\mathbf{s_e}'$ depends of the position vector, and can require a specific treatment for its evaluation in order to ensure the conservativity of its field at the discrete level [8]. A lack of precision is also to be expected for coarse parts of the mesh where the cell size is bigger, as can usually be observed in the far-field. Another source for this difference between the near-field and far-field values in FFX could be coming from the trace of numerical dissipation due to the scheme used in the numerical simulation performed with elsA. It would then be interesting to evaluate the effect of a change of mesh and numerical scheme on the difference between near-field and far-field results.

3. Sensitivity to control volume modifications

In this precision study, it is also interesting to evaluate the different evolutions of the exergy balance terms when modifying the control volume concerned for the post-processing at a fixed $x_{TP} = 0.2m$. To do so, for a fixed lower value $x = x_{min}$, the radius varies from $R_{limit} = 2.0m$ until R_{max}. Then, with $R_{limit} = R_{max}$, the minimum value of x evolves between $x_{limit} = x_{min}$ and $x_{limit} = -2.0m$. The evolution of the exergy balance coefficients is presented using the absolute difference computed as $\xi_{C_\epsilon} = C_\epsilon - C_{\epsilon_{full}}$ where ϵ_{full} is the quantity computed for the full control volume delimited by $x_{TP} = 0.2m$. The relative difference to this coefficient is also computed as $\sigma_{C_\epsilon} = \frac{C_\epsilon - C_{\epsilon_{full}}}{C_{\epsilon_{full}}}$. The results are shown in Figs. 21 and 22.

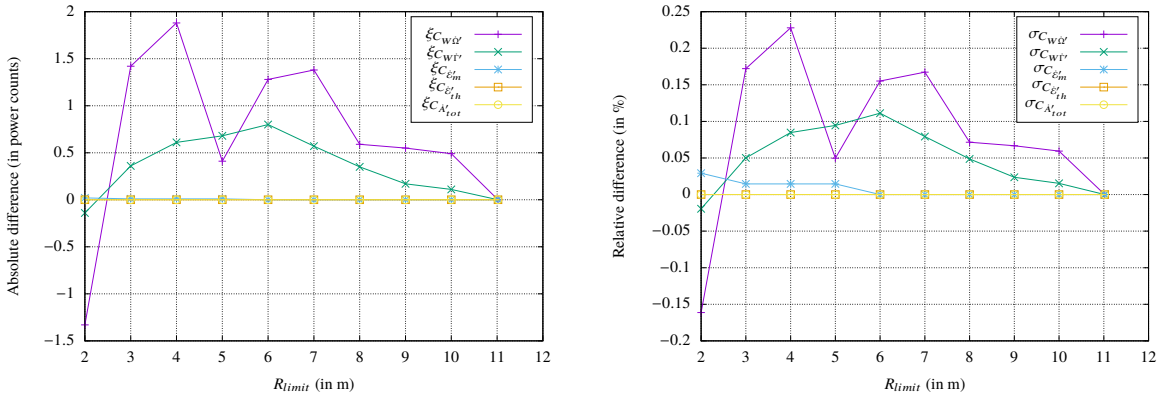

Fig. 21 Evolution of the absolute (left) and relative (right) differences of the exergy coefficients with R_{limit} as compared with the complete control volume value for $x_{TP} = 0.2m$.

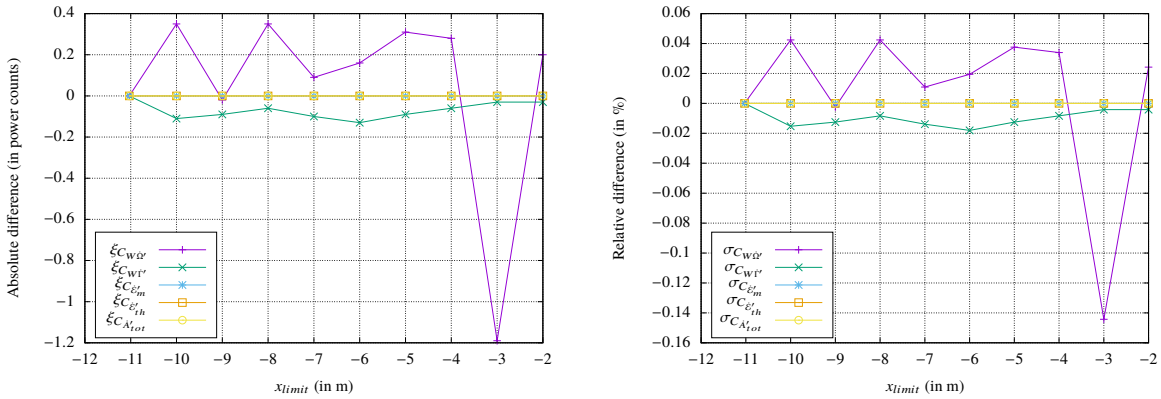

Fig. 22 Evolution of the absolute (left) and relative (right) differences of the exergy coefficients with x_{limit} as compared with the complete control volume value for $x_{TP} = 0.2m$.

These figures show that the variation of the different coefficients is not significant when reducing the control volume radius or in minimum x value. The most notable variations are seen on the $W\dot{\Omega}'$ and $W\dot{\Gamma}'$ coefficients, but always stay below 0.25% of difference with respect to the selected value at minimum x and maximum radius of the grid. This means that the difference between near-field and far-field values for these two coefficients can be slightly influenced by the position of the external boundary, but also that this is not the main reason for it. Hence, this difference should mostly come from other numerical imprecisions due to grid quality or the trace of the dissipation from the numerical scheme in this simulation. Additionally, the evolutions for H^*, S^* and E^* under the same conditions are shown in Fig. 23.

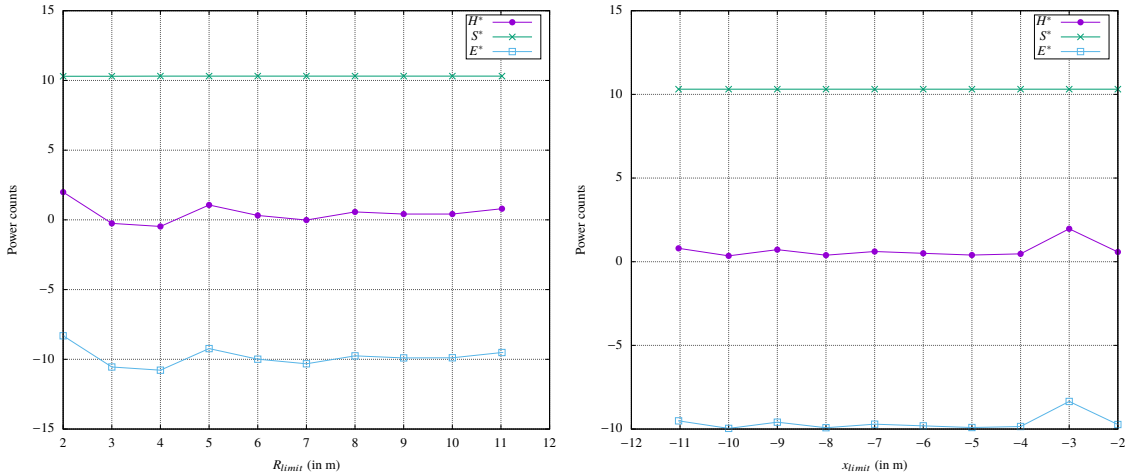

Fig. 23 Evolution of H^*, S^* and E^* with R_{limit} (left) and x_{limit} (right) as compared with the complete control volume value for $x_{TP} = 0.2m$.

Fig. 23 shows that the error on the entropy equation remains constant when x_{limit} and R_{limit} vary. On the other hand, H^* proves to be much more sensitive to these control volume modifications, although its variations stay in the order of magnitude of one power count.

V. Conclusion

This paper presents the theoretical development of an exergy balance adapted to rotating frames of reference and its numerical application to the case of a propeller. This allows to investigate the behavior of the different components of the exergy balance, and to suggest figures of merit to characterize the efficiency of the system under study. Links can also be made between the exergy balance and classical efficiency curves, with supplementary information provided by the maximum efficiency that can theoretically be obtained. Phenomenological links can be made with the exergy balance terms as they allow to vizualize regions of anergy generation and exergy outflow. There is still room for improvement for this formulation in terms of precision, in order to properly account for the residual of the exergy balance at the discrete level. For future works, a next step could also consist in implementing the relative velocity, relative frame formulation inside FFX in order to compare the supplementary information that the balance would provide. Finally, more cases can be studied with this balance such as configurations involving significant thermal exchanges and shockwaves. For example, in the case of a high-pressure compressor or turbine of an aircraft engine, thermal effects cannot be detected by classical analyses based on mechanics, making these approaches incomplete. The exergy balance will then provide additional information on these aspects and the physics involved in it.

Acknowledgments

The work presented in this paper was funded by the French Directorate General for Civil Aviation (DGAC) through the SUBLIME convention. The studies presented have used the elsA software, whose development is partially funded by its three co-owners: ONERA, Airbus, SAFRAN. The authors would also like to thank Itham Salah el Din for providing the test case with the associated mesh for this study and Biel Ortun for his advice and knowledge.

References

[1] van der Vooren, J., and Destarac, D., "Drag/thrust analysis of jet-propelled transonic transport aircraft; Definition of physical drag components," *Aerospace Science and Technology*, Vol. 8, No. 6, 2004, pp. 545–556. https://doi.org/https://doi.org/10.1016/j.ast.2004.03.004, URL https://www.sciencedirect.com/science/article/pii/S1270963804000343.

[2] Destarac, D., "CFD-Based Aircraft Drag Prediction and Reduction," *von Karman Institute for Fluid Dynamics*, 2003.

[3] Drela, M., "Power Balance in Aerodynamic Flows," *AIAA Journal*, 2009. https://doi.org/10.2514/1.42409, URL https://arc.aiaa.org/doi/10.2514/1.42409.

[4] Arntz, A., Atinault, O., and Merlen, A., "Exergy-Based Formulation for Aircraft Aeropropulsive Performance Assessment: Theoretical Development," *AIAA Journal*, Vol. 53, No. 6, 2015, pp. 1627–1639. https://doi.org/10.2514/1.J053467, URL https://doi.org/10.2514/1.J053467.

[5] Arntz, A., "Civil Aircraft Aero-thermo-propulsive Performance Assessment by an Exergy Analysis of High-fidelity CFD-RANS Flow Solutions," Ph.D. thesis, Lille 1 University - Sciences and Technologies, 2014. https://doi.org/10.13140/2.1.3128.1444, URL http://www.theses.fr/2014LIL10110.

[6] Petropoulos, I., Wervaecke, C., Bailly, D., and Derweduwen, T., *Numerical investigations of the exergy balance method for aerodynamic performance evaluation*, 2019. https://doi.org/10.2514/6.2019-2926, URL https://arc.aiaa.org/doi/abs/10.2514/6.2019-2926.

[7] Fiore, M., "Influence of cavity flow on turbine aerodynamics," Ph.D. thesis, 2019. URL http://www.theses.fr/2019ESAE0013, toulouse, ISAE 2019.

[8] Boniface, J. C., "Calcul d'ecoulements compressibles autour de rotors d'helicopteres en vol stationnaire ou en vol d'avancement par resolution des equations d'euler," Ph.D. thesis, ENSAM, 1995. URL http://www.theses.fr/1995ENAM0037.

[9] Kozuch, L., "Etude de l'écoulement dans une turbomachine axiale transsonique en présence ou non d'une distorsion amont : Validation d'un outil de simulation et analyse instationnaire," Ph.D. thesis, 2002. URL http://www.theses.fr/2002ECDL0011, thèse de doctorat dirigée par Ferrand, Pascal Mécanique des fluides Ecully, Ecole centrale de Lyon 2002.

[10] Cengel, Y., and Boles, M., *Thermodynamics: An Engineering Approach.*, 2015. 8th edition, McGraw-Hill.

[11] Meheut, M., *Multidisciplinary Adjoint-based Optimizations in the MADELEINE Project: Overview and Main Results*, 2021. https://doi.org/10.2514/6.2021-3052, URL https://arc.aiaa.org/doi/abs/10.2514/6.2021-3052.

[12] Ortun, B., "A coupled RANS/lifting-line analysis for modelling the aerodynamics of distributed propulsion," *AHS Aeromechanics & Design for Transformative Vertical Flight*, 2018.

[13] Fischer, J.-S., and Ortun, B., "Simulation & Analysis of the Aerodynamic Interactions between Distributed Propellers and Wings," *AHS Aeromechanics & Design for Transformative Vertical Flight*, 2018.

[14] Cambier, L., Heib, S., and Plot, S., "The Onera elsA CFD software: input from research and feedback from industry," *Mechanics & Industry*, Vol. 14, No. 3, 2013, pp. 159–174. https://doi.org/10.1051/meca/2013056, URL https://doi.org/10.1051/meca/2013056.

[15] Benoit, C., Péron, S., and Landier, S., "Cassiopee: A CFD pre- and post-processing tool," *Aerospace Science and Technology*, Vol. 45, 2015, pp. 272–283. https://doi.org/https://doi.org/10.1016/j.ast.2015.05.023, URL https://www.sciencedirect.com/science/article/pii/S1270963815001777.

[16] Meheut, M., *Thrust and Torque Far-field Analysis of Propeller and Counter Rotating Open Rotor Configurations*, 2013. https://doi.org/10.2514/6.2013-2803, URL https://arc.aiaa.org/doi/abs/10.2514/6.2013-2803.

[17] Verley, S., "Evaluation du couple 'champ lointain' d'un rotor d'hélicoptère en vol stationnaire : analyse de résultats issus de simulations numériques de mécanique des fluides," Ph.D. thesis, 2012. URL http://www.theses.fr/2012ORLE2087, Université d'Orléans 2012.